

**Structure of Reduced Cerium Oxide Ultrathin films on Pt(111): Local Atomic Environment and Long-range Order**

Pelli Cresi, J.; Znaiguia, R.; Carlà, F.; Isern, H.; Benedetti, F.; Gasperi, G.; Amidani, L.; Valeri, S.; Boscherini, F.; Luches, P.;

Originally published:

July 2020

**Advanced Materials Interfaces 7(2020)18, 2000737**

DOI: <https://doi.org/10.1002/admi.202000737>

Perma-Link to Publication Repository of HZDR:

<https://www.hzdr.de/publications/Publ-30953>

Release of the secondary publication  
on the basis of the German Copyright Law § 38 Section 4.

# Structure of Reduced Cerium Oxide Ultrathin films on Pt(111): Local Atomic Environment and Long-range Order

Jacopo Stefano Pelli Cresi,<sup>1,2</sup> Francesco Carlà,<sup>3</sup> Raja Znaiguia,<sup>3</sup> Helena Isern,<sup>3</sup> Francesco Benedetti,<sup>1,2</sup> Gabriele Gasperi,<sup>1,2</sup> Lucia Amidani,<sup>3,⊥</sup> Sergio Valeri,<sup>1,2</sup> Federico Boscherini,<sup>4,5</sup> Paola Luches<sup>2\*</sup>

<sup>1</sup> Dipartimento di Scienze Fisiche Informatiche e Matematiche, Università degli Studi di Modena e Reggio Emilia, Via G. Campi 213/a, 41125 Modena, Italy

<sup>2</sup> Istituto Nanoscienze, Consiglio Nazionale delle Ricerche, Via G. Campi 213/a, 41125 Modena, Italy

<sup>3</sup> European Synchrotron Radiation Facility, BP 220, 38043 Grenoble, France

<sup>4</sup> Department of Physics and Astronomy, Alma Mater Studiorum – Università di Bologna, Viale C. Berti Pichat 6/2, 40127 Bologna, Italy

<sup>5</sup> Istituto Officina dei Materiali, Consiglio Nazionale delle Ricerche, OGG, c/o European Synchrotron Radiation Facility, BP 220, 38043 Grenoble, France

\* corresponding author e-mail: [paola.luches@nano.cnr.it](mailto:paola.luches@nano.cnr.it)

⊥ present address: Rossendorf Beamline at the ESRF, HZDR, Institute of Resource Ecology, 01314 Dresden, Germany

**Keywords:** cerium oxide, ultrathin films, x-ray absorption fine structure, x-ray reflectivity, surface x-ray diffraction

## Abstract

To optimize the catalytic functionality of cerium oxide it is important to understand the structural modifications associated with reduction and the role of the proximity of metals, which are often coupled with the oxide in the applications. For this purpose, the evolution of the short- and long-range structure of cerium oxide ultrathin epitaxial films and nanostructures supported on Pt(111) is investigated using x-ray absorption spectroscopy at the Ce L<sub>3</sub> edge and surface x-ray diffraction, during reduction by thermal treatments in vacuum. In epitaxial nanoislands reduction is associated with a contraction of the Ce-O distance and with the appearance of Ce-Pt bonds. The formation of a phase with a (2×2) periodicity after a thermal treatment at 1023 K is ascribed to the formation of a Pt<sub>5</sub>Ce alloy. Films of 3 nm thickness do not show, on average, significant structural modifications with the same thermal treatment, consistent with the hypothesis that the reduction involves only the topmost surface layers and it does not influence significantly the bulk structure of the material. This study demonstrates a strong interaction between cerium oxide and platinum, which has implications for the reactivity and stability of catalysts based on metals combined with reducible oxides.

## 1. Introduction

Due to their catalytic properties reducible oxides are extremely interesting materials for a number of applications.<sup>[1]</sup> The possibility to easily and reversibly release oxygen ions represents in fact a very important functionality, in particular when these compounds are used as supports for metal catalysts. Understanding the structural modifications associated with reduction and the role of metal/oxide interfaces is important in view of designing materials with improved reducibility. Cerium oxide represents a prototypical reducible oxide and its most stable bulk phase is  $\text{CeO}_2$  with a fluorite-type structure, in which the Ce ions in the 4+ oxidation states are arranged in an fcc structure and the oxygen ions occupy tetrahedral sites. Under mild reducing conditions oxygen vacancies are progressively formed in  $\text{CeO}_2$ , but the fluorite structure is retained. Significant changes in the structure are induced only if the concentration of  $\text{Ce}^{3+}$  ions is above a few tens percent. If the  $\text{Ce}^{3+}$  concentration is 100%, i.e. in sesquioxide  $\text{Ce}_2\text{O}_3$ , the A-type hexagonal phase is most stable, while the C-type cubic bixbyite phase, obtained from the fluorite structure by removing 25% of oxygen ions from specific lattice sites and by allowing for a slight structural rearrangement, is relatively less stable. At intermediate oxidation degrees a number of metastable phases have been identified.<sup>[2]</sup> The situation is even more complex at reduced dimensionality, i.e. in ultrathin films and nanoparticles, in which more complex structures are expected to be stabilized by reduction and by different substrates.<sup>[3]</sup>

Ultrathin films have often been used as playground to stabilize specific reduced cerium oxide phases, to investigate interfacial interactions and the resulting properties through electron spectroscopy and microscopy techniques. In particular, in the case of cerium oxide the question has been addressed in a number of studies revealing a complex situation, with the substrate playing in general a very relevant role in the stabilization of specific structures.<sup>[4]</sup> Reduced cerium oxide phases can be obtained by evaporating cerium in low oxygen background pressure, obtaining a fluorite structure with vacancies.<sup>[5, 6]</sup> Mild reduction degrees can be obtained by electron bombardment<sup>[7, 8]</sup> or by X-ray irradiation<sup>[9]</sup>, while ion bombardment induces in general a higher concentration of surface oxygen vacancies.<sup>[10]</sup> Controlled degrees of reduction have been obtained by thermal treatments in reducing atmosphere, like for example vacuum<sup>[11-14]</sup> or hydrogen.<sup>[10, 15]</sup> At mild degrees of reduction the surface long-range order of cerium oxide films, as probed by low energy electron diffraction (LEED), is not substantially altered, suggesting that the reduction proceeds by the formation of oxygen vacancies at random sites within the cerium oxide fluorite structure.<sup>[11]</sup> At specific degrees of reduction the formation of ordered arrays of oxygen vacancies has been observed both in direct space using scanning tunneling microscopy<sup>[16-18]</sup> and in reciprocal space using LEED.<sup>[6, 13, 14, 17, 19]</sup> In some cases, the reconstruction was observed only on ultrathin films and ascribed to a lower oxygen vacancy formation energy in different sites of the film-substrate coincidence cell.<sup>[13, 16, 18]</sup> This is the case of the  $(5 \times 5)$  superstructure, observed for ultrathin cerium oxide films on  $\text{Rh}(111)$ <sup>[11]</sup> and  $\text{Pt}(111)$ <sup>[20]</sup> and possibly also of the  $(3 \times 3)$ <sup>[18]</sup> and  $9/4(\sqrt{3} \times \sqrt{3})$ ,<sup>[13]</sup> observed on  $\text{Pt}(111)$ . In other cases, well defined phases, metastable in the bulk, were stabilized on different substrates and at different thickness. An example is the  $\text{Ce}_7\text{O}_{12}$  i-phase,

identified by the occurrence of a  $(\sqrt{7} \times \sqrt{7})$  R19.1° reconstruction in the LEED patterns on Si(111),<sup>[21]</sup> as well as on Cu(111)<sup>[17]</sup> and on Pt(111).<sup>[9]</sup> Other structures with surface periodicity ascribed to “quasistable” bulk phases like the  $(3 \times 3)$  one<sup>[22]</sup> were obtained on different substrates like Cu(111),<sup>[17]</sup> Ru(0001)<sup>[15]</sup> and Pt(111).<sup>[13, 20]</sup> At high Ce<sup>3+</sup> concentrations in some cases the cubic C-type phase, identified by a  $(4 \times 4)$  surface periodicity, was observed.<sup>[14, 15, 17, 23]</sup> The structural transformations were often shown to be reversible by treatments in oxidizing conditions, which transform the films back to the fluorite CeO<sub>2</sub> phase.<sup>[9, 13, 17]</sup>

The complexity and variety of the possible reduced ceria phases in ultrathin films is pointed out also by a theoretical work by Kozlov et al., which interestingly predicts that different structures can gain stability by very small changes of the surface lattice parameter and that phases which do not exist in the bulk form can have a comparable stability as the A-type or the C-type phases.<sup>[3]</sup>

X-ray absorption fine structure (XAFS) is a powerful experimental tool, which allows to precisely determine the local structure surrounding a specific atom in a compound, and to simultaneously determine its chemical state. It has often been applied to cerium-oxide based systems to correlate structural modifications to reduced dimensionality<sup>[24, 25]</sup> or to the interaction with metals.<sup>[26]</sup>

Surface X-ray diffraction (SXRD) allows to study the crystal structure of surfaces and thin layers. It is extremely sensitive to changes of the surface long-range order and it has often been used to detect minor changes in the surface lattice parameter in ultrathin films and in different environments.<sup>[27]</sup> Remarkably, the technique has allowed to identify the coexistence of a dominant hexagonal A-type Ce<sub>2</sub>O<sub>3</sub> phase and of a minority C-type Ce<sub>2</sub>O<sub>3</sub> phase after prolonged vacuum reduction of cerium oxide epitaxial structures.<sup>[28]</sup>

In the present work we investigate the local atomic environment of Ce ions and the long-range structural order in cerium oxide epitaxial films on Pt(111) and their modification during thermal reduction in vacuum. The study is performed using Ce L<sub>3</sub>-edge XAFS measurements in the near and extended energy ranges, which allow to correlate the chemical and the structural modifications, in combination with SXRD and X-ray reflectivity (XRR) measurements, which give complementary information on the evolution of the film structure and morphology.

## 2. Experimental

The samples here investigated are three cerium oxide films, grown on a Pt(111) single crystal in an ultrahigh vacuum experimental chamber. The substrate was cleaned by repeated cycles of Ar<sup>+</sup> sputtering (1 keV, 1 μA/cm<sup>2</sup>) and annealing at 1040 K, until the surface showed a sharp  $(1 \times 1)$  LEED pattern and the signal from contaminants was below the detection limit of X-ray photoemission spectroscopy. The cerium oxide films were grown by reactive molecular beam epitaxy, namely evaporation of metallic cerium from an electron bombardment cell (evaporation rate = 0.5 Å/min, evaluated by a quartz microbalance) in an oxygen pressure

of  $1 \times 10^{-7}$  mbar. The Pt substrate was kept at room temperature during cerium oxide evaporation. Two of the samples, of nominal thickness 2 and 10 monolayers (MLs), were annealed at 1040 K in an  $O_2$  partial pressure of  $1 \times 10^{-7}$  mbar after the growth, to induce a regular morphology and a good crystal quality as demonstrated in previous works by STM and LEED<sup>[19]</sup>. The LEED images of the samples here investigated, reported in the supporting information as Figure S1, confirm the epitaxial orientation between the films and the substrate as  $CeO_2(111) // Pt(111)$  and  $CeO_2[110] // Pt[110]$ . The samples treated in  $O_2$  after the growth will be referred to as “epitaxial” in the following. We note that in the 2 ML film the thermal treatment induced a partial dewetting of the Pt substrate surface and lead to the formation of bilayered epitaxial islands with flat surfaces of several tens of nm lateral size, as shown in reference [13]. A third sample of 2 ML nominal thickness, referred to as “as-grown”, was prepared without the post-growth annealing treatment and it showed a surface with grains of nanometric size and a high density of undercoordinated sites, as shown in previous works by STM.<sup>[19]</sup> The crystal quality of this sample is worse than the one of the 2 ML epitaxial sample, as shown by the LEED patterns in Figure S1. We emphasize that 2 ML and 10 ML correspond to nominal thickness values, derived from the amount of cerium oxide deposited, in turn evaluated as the product of the evaporation rate and the deposition time. 1 ML corresponds to the thickness of the repeating unit along the [111] direction, i.e. an O-Ce-O trilayer (3.12 Å). The effective height of the films may actually be different due to sticking coefficient, desorption and ripening induced by the thermal treatment.

The XAFS experiment at the Ce  $L_3$  edge was performed at the LISA BM08 beamline<sup>[29]</sup> of the European Synchrotron Radiation Facility (ESRF) in Grenoble. The lineshape of Ce  $L_3$ -edge in the X-ray absorption near edge spectroscopy (XANES) region is very sensitive to modifications of the oxidation state and the local electronic structure, while analysis of the extended X-ray absorption fine structure (EXAFS) part of the spectrum provides information on the local atomic structure around Ce ions. The measurements were performed using a dynamically sagittal-focusing Si(311) monochromator<sup>[30]</sup> coupled to a pair of Pt-coated mirrors to remove higher-order harmonics.

The samples were carried to the ESRF in a non-reactive  $N_2$  atmosphere. Two reference samples were also measured: a  $CeO_2$  powder sample ( $Ce^{4+}$  reference) and a cerium silicate film ( $Ce^{3+}$  reference), grown following the procedures described in reference<sup>[31]</sup>. The cerium oxide films were mounted in a high-temperature furnace (Micro-Tomo from the ESRF Sample Environment Support Department), which was installed in the BM08 acquisition chamber and used to apply *in-situ* thermal treatments to the sample in high vacuum (HV) conditions ( $P \sim 10^{-7}$  mbar). The same setup was previously shown to induce partial reduction in cerium oxide films and nanoparticles.<sup>[32, 33]</sup>

The samples were measured in the fluorescence yield mode using a single element detector, the solid angle of detection being limited by the furnace window. This limitation, together with the low thickness of the ceria films, made the measurements very challenging. Ce  $L_3$ -edge spectra in the near and extended energy range

were acquired before and after a reducing thermal treatment in HV at 1023 K. The CeO<sub>2</sub> powder was measured in the transmission mode, while the thin silicate film was measured in the fluorescence mode.

The analysis of the XANES spectra was performed by an empirical fitting procedure, following reference <sup>[34]</sup>, as reported in detail in the Supporting Information, Figure S2. The spectra were normalized to the step edge and fitted with five Gaussian curves, one related to Ce<sup>3+</sup>, three related to Ce<sup>4+</sup> and one for the pre-edge peak. The step edge was simulated using an arctangent function with the maximum of the first derivative fixed to the value of the first derivative of the experimental spectrum. The relative area and distance of the three Ce<sup>4+</sup>-related components were fixed for all samples to the values obtained from the fit of the Ce<sup>4+</sup> reference sample. The Ce<sup>3+</sup> concentration was evaluated as the ratio of the area of the Ce<sup>3+</sup>-related peak and the total area of the XANES. Since it was not possible to resolve the Ce<sup>3+</sup> and Ce<sup>4+</sup> contributions to the pre-edge peak, <sup>[35]</sup> its intensity was not considered in the evaluation of the concentration of the two different oxidation states. The error on the Ce<sup>3+</sup> concentration given by the fit is of the order of 10%.

The EXAFS data were analyzed using the Demeter suite, <sup>[36]</sup> which includes ATHENA for the extraction of the EXAFS function and ARTEMIS for its fitting. The theoretical signals used in the fitting were generated by the FEFF6 program. <sup>[37]</sup> The analysis was limited, in most cases, to the first coordination shell using single scattering paths relative to the fluorite CeO<sub>2</sub> structure. In selected cases a linear combination of contributions from CeO<sub>2</sub> and Ce alloys was used, as described below. During the fitting procedure the Ce-O distance, the Debye-Waller (DW) factor ( $\sigma^2$ ) and energy origin shift were used as free fitting parameters, while  $S_0^2$  was kept fixed to the value obtained from the fitting of the CeO<sub>2</sub> reference sample; the fits were performed in reciprocal space on the Fourier-filtered signal. Given the limited k range available for the analysis, the presence of multiple excitations and the mixed-valence nature of the excited state <sup>[38, 39]</sup> were neglected, considering also the expected weak intensity of the related features.

The XRR and SXRD measurements were performed at the ID03 beamline of the ESRF, using a z-axis diffractometer, operating in horizontal scattering geometry, equipped with a UHV system. The incident photon beam, with an energy of 24 keV, was focused to 30  $\mu\text{m}$  x 200  $\mu\text{m}$  at the sample position. The data were collected using a MAXIPIX area detector located at a distance of 961 mm from the sample.

The two ceria samples of 2 ML and 10 ML thickness used for the XRR and SXRD were grown on Pt(111) using the same procedures used for the samples for the XAS measurements, including the post-growth thermal treatment in oxygen partial pressure, and carried to the ESRF in non-reactive atmosphere. The samples were transferred in the UHV chamber of the diffractometer (base pressure  $5 \times 10^{-9}$  mbar) and cleaned by annealing in O<sub>2</sub> partial pressure ( $T = 673$  K,  $P_{\text{O}_2} = 10^{-7}$  mbar), to remove surface contamination due to the short air exposure during sample mounting. Subsequently, they were treated by reducing/oxidizing cycles. The reducing treatments were performed at different temperatures (573 K, 773 K and 1023 K) in UHV ( $10^{-9}$  mbar). The samples were kept at each temperature step for 30 minutes and let cool down to room temperature

before the measurements. The structure of the samples after each temperature step was characterized by SXRD and XRR. Auger electron spectroscopy was used to check in-situ the evolution of the sample surface composition after each temperature step. Reciprocal space maps were analysed using the BINoculars software.<sup>[40]</sup> For convenience, all the reciprocal space positions are referred to the surface unit cell of the Pt(111) substrate ( $a=b=2.775 \text{ \AA}$ ,  $c=6.797 \text{ \AA}$ ,  $\alpha=\beta=90^\circ$ ,  $\gamma=120^\circ$ ).

### 3. Results and discussion

#### 3.1 XANES and EXAFS results

The XANES spectra acquired on all samples are reported in Figure 1. The thermal treatment significantly affects the lineshape of the two 2 ML samples, inducing a shift towards lower energy of the edge and an overall change, clearly indicating a partial reduction of the films. The spectral changes for the 10 ML sample are less pronounced, possibly because thermal reduction of the films affects mainly the sample surface, while the fluorescence yield detection mode probes the full thickness of the films.

To obtain quantitative information on the concentration of  $\text{Ce}^{4+}$  sites in the samples, the spectra were fitted with components ascribed to the two ionic species, as described in the previous section (see also Figure S2 in the Supporting Information for further details). The results of the fitting procedure are reported in Tab. 1. Before reduction, the  $\text{Ce}^{4+}$  concentration in the 2 ML as-grown film is significantly lower (77 %) than in the 2 ML epitaxial sample (90 %). This difference is induced by the post-growth thermal treatment in oxygen undergone by the epitaxial sample.<sup>[19]</sup> The small but non-negligible  $\text{Ce}^{3+}$  concentration detected in the two 2 ML samples before reduction (10 % and 23 % for the epitaxial and as-grown films, respectively) can be ascribed to the presence of a residual density of low coordination sites, and to some charge transfer from the Pt substrate.<sup>[41]</sup>

Both a visual inspection of the spectral changes (Figure 1) and the results of the fitting procedure (Table 1), indicate that after the reducing treatment the 2 ML epitaxial sample has a slightly lower  $\text{Ce}^{4+}$  concentration (52 %) than the 2 ML as-grown sample (56 %). This result is, at first glance, surprising because the as-grown film has a higher concentration of low coordinated cerium sites and it is therefore expected to exhibit a higher reducibility compared to the epitaxial one. Moreover, the 2 ML epitaxial sample exposes mostly (111) surfaces for which the formation energy of oxygen vacancies is higher than for the other low index surfaces.<sup>[42]</sup> The slightly lower concentration of  $\text{Ce}^{4+}$  in the epitaxial film can be rationalized by considering that the thermal treatment in oxygen undergone by the 2 ML epitaxial sample induces the formation of 3-4 ML high islands, which do not totally cover the Pt substrate.<sup>[13]</sup> The 2 ML as-grown sample instead covers

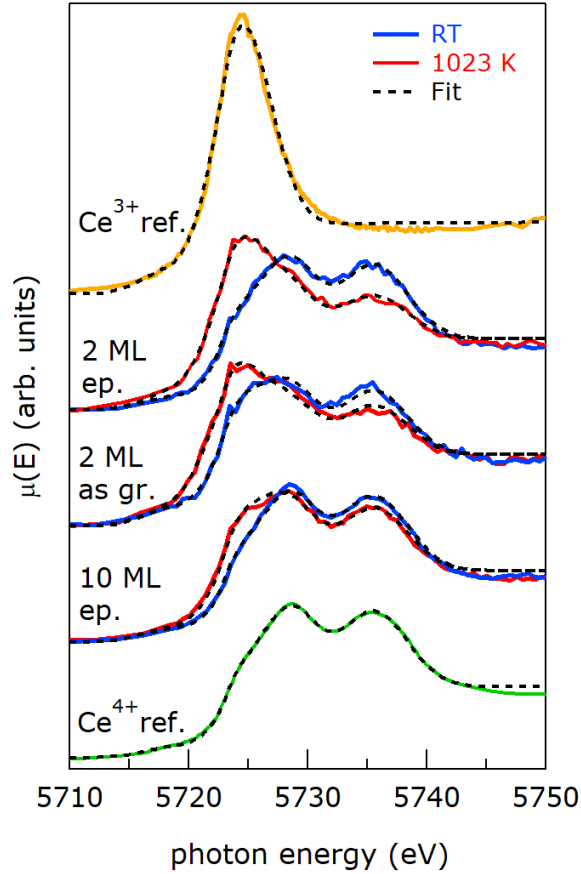


**Figure 1.** Ce L<sub>3</sub>-edge XANES spectra for 10 ML epitaxial, 2 ML as-grown and 2 ML epitaxial ceria samples before (blue lines) and after (red lines) the reducing treatment. The spectra are compared to Ce<sup>4+</sup> (CeO<sub>2</sub>, yellow line) and Ce<sup>3+</sup> (Ce silicate, green line) references. The fits are shown as black dashed lines.

almost uniformly the Pt substrate<sup>[19]</sup>. It must be noted that the formation of oxygen vacancies may be favored at the edge sites of the cerium oxide islands, present in the annealed film, because of their reduced coordination and of the proximity of Pt atoms, which possibly induce a decrease of the formation energy of oxygen vacancies by charge transfer<sup>[41]</sup> or by interatomic exchange processes.<sup>[43]</sup> The 2 ML as-grown sample has a much lower density of Pt-ceria edge sites compared to the 2 ML epitaxial sample. The morphology and the interaction with the substrate are likely to play a more important role than the surface defectivity, effectively contributing to the observed higher reducibility of the 2 ML epitaxial film compared to the 2 ML as-grown one. We note that the shape of the Ce L<sub>3</sub>-edge spectra of trivalent metallic Ce phases, and of CePt alloys in particular, do not differ significantly from the one of Ce<sup>3+</sup> phases, apart from a shift of the edge

position of about 2 eV.<sup>[44]</sup> The energy resolution of the technique does not allow to distinguish the individual contributions of metallic Ce and Ce<sup>3+</sup> as minority components of the XANES spectra of the samples after the

		C <sub>Ce<sup>4+</sup></sub> (%)	C <sub>Ce<sup>3+</sup></sub> (%)	C <sub>Ce<sup>3+</sup> + C<sub>Ce<sup>met</sup></sub></sub> (%)
2 ML epitaxial	RT	90	10	-
	1023 K	52	-	48
2 ML as-grown	RT	77	23	-
	1023 K	56	-	44
10 ML epitaxial	RT	94	6	-
	1023 K	76	-	24

**Table 1.** Ce<sup>4+</sup> and Ce<sup>3+</sup> concentration obtained from the fitting of the XANES spectra before and after the thermal treatment in vacuum at 1023 K. After the thermal treatment the component not related to Ce<sup>4+</sup> is ascribed both to Ce<sup>3+</sup> and to possible metallic Ce phases.



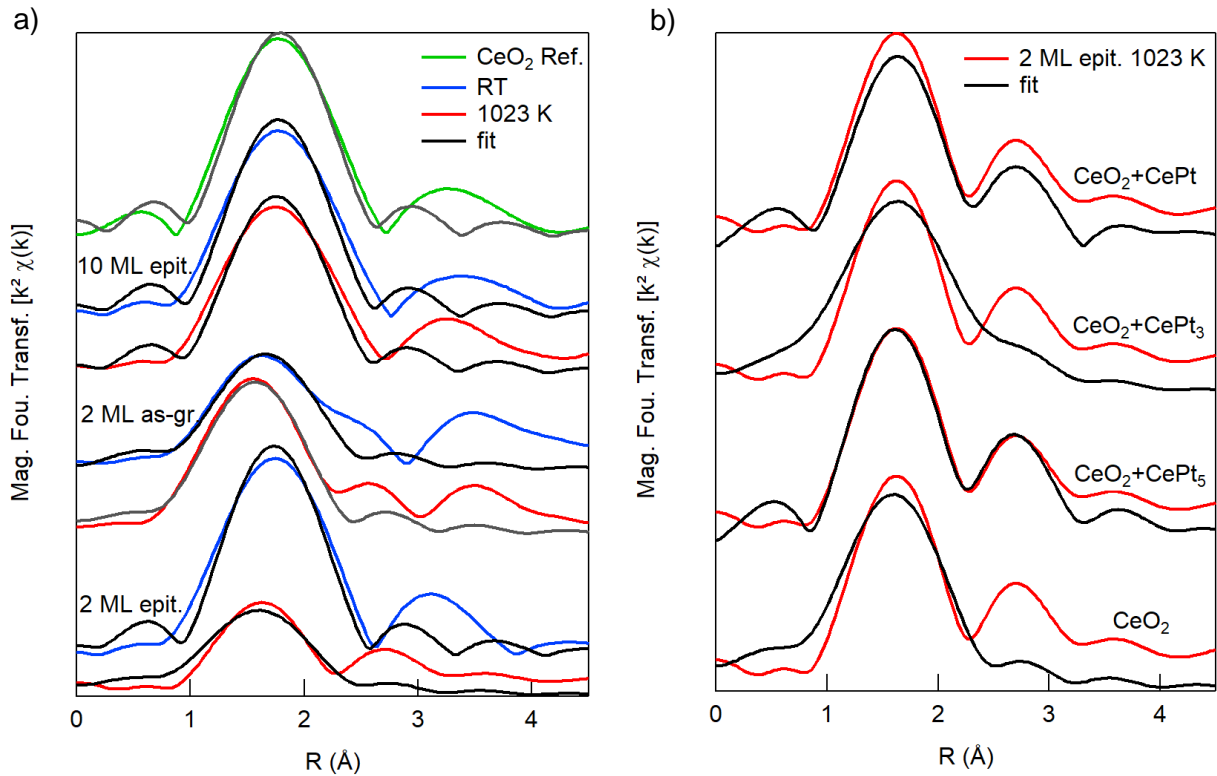


**Figure 2.** a) Magnitude of the Fourier transform of  $k^2$ -weighted  $\chi(k)$  measured before (blue lines) and after (red lines) the reducing treatment. The black lines are the fits using first shell Ce-O scattering paths. b) Comparison between the Fourier transform of the epitaxial 2 ML after the thermal treatment and different fits using a Ce-O path from CeO<sub>2</sub> and an additional Ce-Pt path from different Ce-Pt alloys.

thermal treatment. We therefore consider that an unknown fraction of the Ce phase not related to Ce<sup>4+</sup> after reduction may be ascribed to a metallic alloyed phase, based also on the analysis of EXAFS, XRR and SXRD data described in the following.

The EXAFS data were analysed up to  $k = 6.5 \text{ \AA}^{-1}$ ; this limited  $k$  range is due the relatively weak signal provided by the very low thickness of the films. Therefore, the data analysis was limited to the first coordination shell in most cases. For fluorite CeO<sub>2</sub> the first shell consists in eight O atoms at a distance of  $2.34 \text{ \AA}$ . With this limited  $k$  range the strong correlation between coordination number and DW factor, a well-known limitation of EXAFS analysis, made it impossible to determine both parameters reliably. For this reason, in the analysis we fixed the coordination number to eight, as in fully coordinated Ce ions in CeO<sub>2</sub>.

Thus, the variations in the DW factors determined by our analysis may reflect in part also changes in the coordination number. In spite of this limitation, the approach used allowed to have reliable information on important modifications of the Ce local environment in the films during the thermal reduction treatment.

Figure 2 (a) reports the magnitude of the Fourier transforms of the  $k^2$ -weighted EXAFS function  $\chi(k)$  and the corresponding fits for the three films before (blue lines) and after (red lines) the reducing treatment. The

Sample	R-factor	$S_0^2$	N	R (Å)	$\sigma^2$ (Å <sup>2</sup> )
CeO <sub>2</sub>				2.34	
CeO <sub>2</sub> ref.	0.009	0.70(18)	8	2.29 (3)	0.003(6)
10 ML epitaxial RT	0.010	0.70	8	2.29 (3)	0.003 (2)
10 ML epitaxial 1023 K	0.010	0.70	8	2.28 (3)	0.006 (2)
2 ML epitaxial RT	0.010	0.70	8	2.26 (3)	0.002 (2)
2 ML epitaxial 1023 K	0.028	0.70	8	2.22 (6)	0.019 (4)
2 ML epitaxial 1023 K + Pt	0.005	0.70	1-A=0.5(1) A=0.5(1) Ce-O 8 Ce-Pt 18	2.24 (2) 3.31(3)	0.004 (2)
2 ML as-grown RT	0.014	0.70	8	2.24 (5)	0.014 (3)
2ML as-grown 1023 K	0.019	0.70	8	2.22 (4)	0.011 (4)
2 ML as-grown 1023 K + Pt	0.019	0.70	1-A=0.6(3) A=0.4(3) Ce-O 8 Ce-Pt 18	2.23 (6) 3.25(12)	0.002 (7)

**Table 2.** R-factor, amplitude reduction factor ( $S_0^2$ ), coordination number (N), Ce–O first-neighbor distances (R), and DW factor ( $\sigma^2$ ) obtained from the fits of the EXAFS spectra at RT and after the thermal treatment at 1023 K. “+Pt” indicates the use of a Ce-Pt scattering path with a weight A in the fit. The numbers in brackets indicate the standard deviation on the last or last two digits. The first row reports the Ce-O distance in bulk cerium oxide for comparison.

spectrum and the fit of the CeO<sub>2</sub> reference sample are also reported for comparison. The results obtained from the fits are reported in Table 2. The Ce-O distance which results from the analysis of the EXAFS spectrum of the CeO<sub>2</sub> reference sample in the 3 - 10 Å<sup>-1</sup> k-range is compatible with the one of bulk CeO<sub>2</sub>, reported in Table 2 (see also Supporting Information, Figure S3). For comparison with the results of the fitting of XAFS data acquired on the films, the CeO<sub>2</sub> reference sample spectrum was also analyzed in the limited k-range, introducing an error on the absolute value of the Ce-O distance which results from the fitting (Table 2).

In the 10 ML epitaxial film before the thermal treatment the Ce-O distance is consistent with the one measured on the reference CeO<sub>2</sub> sample, analyzed in the same k-range, in agreement with a fully relaxed fluorite structure, as already observed in previous work.<sup>[24]</sup> A contraction in the Ce-O distance of a few percent is observed in the 2 ML epitaxial sample as compared with the 10 ML epitaxial film. The contraction of the interatomic distance, already observed in a previous work on similar films,<sup>[19, 24]</sup> can be ascribed to the presence of an epitaxial compression at low thickness, and to its relaxation above a few ML. The 2 ML as-grown film also shows a Ce-O distance smaller than the 10 ML film and comparable to the epitaxial one (Table 2). In the as-grown sample the crystalline order is certainly worse than the one obtained after the thermal treatment in oxygen,<sup>[19]</sup> nevertheless some substrate-induced contraction is possibly already present after the growth at room temperature. An alternative explanation for the observed contraction could be the smaller Ce-O distance at reduced dimensionality, which was theoretically predicted<sup>[45]</sup> and experimentally verified<sup>[33]</sup> for CeO<sub>2</sub> nanoparticles. As expected, the DW factor is higher in the 2 ML as-grown film compared to the 2 ML epitaxial sample, due to the increased structural disorder.

In the 10 ML epitaxial film after the reducing treatment the Ce-O distance does not show a significant modification. For the same film, the DW factor shows an increase after reduction, probably reflecting a decrease in the average coordination number, due to the formation of oxygen vacancies induced by the vacuum thermal treatment. The slight modifications observed in the 10 ML film after reduction are consistent with the minor changes observed in the XANES spectra of the same sample (figure 1). The 2 ML epitaxial film shows a slight contraction of the Ce-O distance and a significant increase of the DW factor after the reducing treatment. The latter can be explained by considering the relatively high  $\text{Ce}^{3+}$  concentration, deduced from the fitting of the XANES spectra (53%), which implies a lower average coordination number of Ce ions after reduction.

The small contraction of the Ce-O distance, observed after the thermal treatment for both the 2 ML epitaxial and the 2 ML as grown sample is unexpected, since the increase of  $\text{Ce}^{3+}$  concentration upon reduction should result in a higher average value of the Ce – O distance due to the larger ionic radius of  $\text{Ce}^{3+}$  compared to  $\text{Ce}^{4+}$ .

To explain the apparent inconsistency, we hypothesize the formation of a Ce-Pt alloy with the reducing treatment at 1023 K. In the literature the formation of metallic CePt alloys has already been observed by LEED, LEEM and STM/AFM after a significant film reduction.<sup>[43, 46-48]</sup> In order to explore this possibility, the EXAFS data of the 2 ML samples after reduction were fitted using a Ce-Pt scattering path with a weight  $A$ , in addition to the Ce-O one with a weight  $1-A$ , with  $A$  used as a free fitting parameter. We chose three possible candidates as the most probable alloys formed by the high temperature treatment:  $\text{CePt}$ ,<sup>[49]</sup>  $\text{CePt}_3$ <sup>[50]</sup> and  $\text{CePt}_5$ .<sup>[51]</sup> The unit cells and the first shell distances are reported in the Supporting Information (Figure S4 and Table S1). To limit the number of fitting parameters, the coordination shells closer than 0.4 Å were considered as a single shell. The Ce-Pt path of the alloy was introduced in the fit of the experimental data of the 2 ML epitaxial and as-grown samples after the reducing treatment. The results of the fitting procedure for the different alloys are reported in Figure 2 (b), which shows that, among the considered alloys,  $\text{CePt}_5$  gives the best fit of the experimental data. The quality of the fit is significantly improved by introducing a Ce-Pt scattering path; the resulting parameters are shown in Table 2. For both the 2 ML epitaxial and 2 ML as-grown samples the contraction of the first Ce-O shell is confirmed and the final distance of the Ce-Pt shell matches quite well with the weighted mean of the first two Ce-Pt shells of the  $\text{CePt}_5$  alloy. The limited  $k$  range reduces the accuracy of this analysis, which nevertheless can be considered as a reliable indication of the formation of a Ce-Pt alloy with the reduction treatment. The larger weight of the alloy scattering path in the epitaxial sample as compared to the as-grown sample (table 2) suggests a higher degree of interatomic exchange in the former, possibly induced at the edges between cerium oxide islands and Pt. This result is qualitatively consistent with the evidence for a higher concentration of reduced phases ( $\text{Ce}^{3+}$  + metallic Ce) observed in the XANES of the 2 ML epitaxial sample as compared to the as-grown one.

Based on the hypothesis of the transformation of part of the oxide into a  $\text{CePt}_x$  alloy by the reducing treatment, it is possible to make some considerations on the decrease of the Ce – O distance. The formation of the alloy at the step edge of the islands reduces their lateral size. This behavior has been already observed in previous works by LEEM<sup>[43]</sup> and AFM.<sup>[48]</sup> The decrease of the lateral size of cerium oxide islands is also reflected in the reduction of the first shell intensity in the Fourier transform (Figure 2 a) after the reducing treatment. This drop-in intensity is quantified by the increase of the apparent DW factor (as reported in table 2). Some theoretical works have predicted a contraction of the lattice parameter for very small clusters of  $\text{CeO}_2$ ,<sup>[45, 52]</sup> which was confirmed experimentally.<sup>[33]</sup> Therefore, the observed contraction of the Ce – O distance can be explained as a dimensionality effect generated by the shrinking of cerium oxide islands after the formation of a cerium-platinum alloy.

### 3.2 XRR and SXRD results

Cerium oxide films, comparable in nominal thickness and subjected to similar treatments as those investigated by XAFS, were analyzed by XRR and SXRD to have complementary information on the out-of-plane density profiles and on the in- and out-of-plane long range order.

Figure 3 shows the XRR profiles for the 2 and 10 ML samples after the treatments at increasing temperatures. The thicker film shows marked intensity oscillations, which are not significantly altered by the thermal treatments. On the contrary, the 2 ML sample does not show any evident periodic oscillation. The XRR curves were modelled and fitted using the GenX software;<sup>[53]</sup> the film thickness and the interface roughness for both film and substrate were used as free parameters in the fitting (the best fit parameters are listed in Table 3). The results obtained for the 10 ML sample indicate a fairly low substrate roughness, a much higher film surface roughness and an average film thickness of 27.0 Å (Table 3), which is close to the nominal thickness of 10 ML = 31.2 Å, obtained using the evaporation rate measured by the quartz microbalance. The film is rather stable after the thermal treatments, which do not significantly alter the thickness, density and surface roughness (Table 3)..

The interpretation of the data for the 2 ML sample is not as straightforward as for the 10 ML sample. This is probably due to the morphology of the sample, made of oxide islands covering a fraction of the substrate.<sup>[13, 19]</sup> The XRR profile before the reducing treatments was fitted in the region  $0.3 \text{ Å}^{-1} < q_z < 1.2 \text{ Å}^{-1}$  and using a starting film thickness of 5.4 Å, equivalent to 1/5 of the thickness evaluated by XRR for the nominally 10 ML thick film. The fitting converged to film thickness values that are significant smaller than the starting value ( $\sim 3 \text{ Å}$ ), probably because the sample has a subnanometric thickness and an island-like morphology,<sup>[13, 19]</sup> which are not considered by the simulation software. Also for this sample the film surface shows a significantly higher roughness than the substrate (Table 3). The reflectivity curves do not show striking differences after the treatments at different temperatures, and their fitting parameters showed also minor changes. It should be noted however that an important piece of information can be extracted from the position of the critical

angle (dashed line in Figure 3b), which shows a significant change after the treatment at 1023 K from 0.085 Å<sup>-1</sup> to 0.072 Å<sup>-1</sup> (from 0.2° to 0.17°). This can be explained by a gradual change in composition and density of the surface, compatible with a transformation from Pt (d=21.45 g/cm<sup>3</sup>) to a Pt<sub>5</sub>Ce alloy (d=16.99 g/cm<sup>3</sup>). The curve after the 1023 K thermal treatment was fitted using a model in which the density of the substrate is left as a free fitting parameter using the Pt<sub>5</sub>Ce density as a starting value: in this condition the fitting converged towards a situation in which the thickness and roughness of the CeO<sub>2</sub> layer are zero.

The formation of the same alloy was observed for metallic Ce layers deposited on the Pt(111) surface and annealed in vacuum at intermediate temperatures in previous papers.<sup>[46, 47, 54]</sup> Evidences of mass exchange processes between cerium oxide films and the Pt substrate under reducing conditions have also been observed by scanning microscopies<sup>[48]</sup> and low energy electron microscopy<sup>[20]</sup> and they are fully consistent with the results of the EXAFS analysis illustrated in section 3.1.

	10 ML			2 ML				
	CeO <sub>2</sub> film thickness (Å)	Pt roughness, $\sigma_{\text{RMS}}$ (Å)	CeO <sub>2</sub> film roughness, $\sigma_{\text{RMS}}$ (Å)	CeO <sub>2</sub> film thickness (Å)	Pt roughness, $\sigma_{\text{RMS}}$ (Å)	CeO <sub>2</sub> film roughness, $\sigma_{\text{RMS}}$ (Å)	Substrate density (g/cm <sup>3</sup> )	Substrate composition
<b>RT</b>	27.0±0.5	0.47±0.14	1.89±0.25	3.1±0.9	0.0±0.19	1.88±0.4	21.45	Pt
<b>523 K</b>	26.9±0.5	0.58±0.11	2.16±0.26	3.4±1.0	0.26±0.21	1.84±0.5	21.45	Pt
<b>773 K</b>	26.6±0.5	0.58±0.15	2.36±0.25	3.0±0.9	0.25±0.21	1.98±0.5	21.45	Pt
<b>1023 K</b>	27.3±0.5	0.52±0.15	2.26±0.23	-	0.8±0.3	-	16.97±0.05	Pt <sub>5</sub> Ce

**Table 3:** Parameters resulting from the fitting of the XRR curves of 2 ML and 10 ML cerium oxide samples after the thermal treatment at different temperatures.

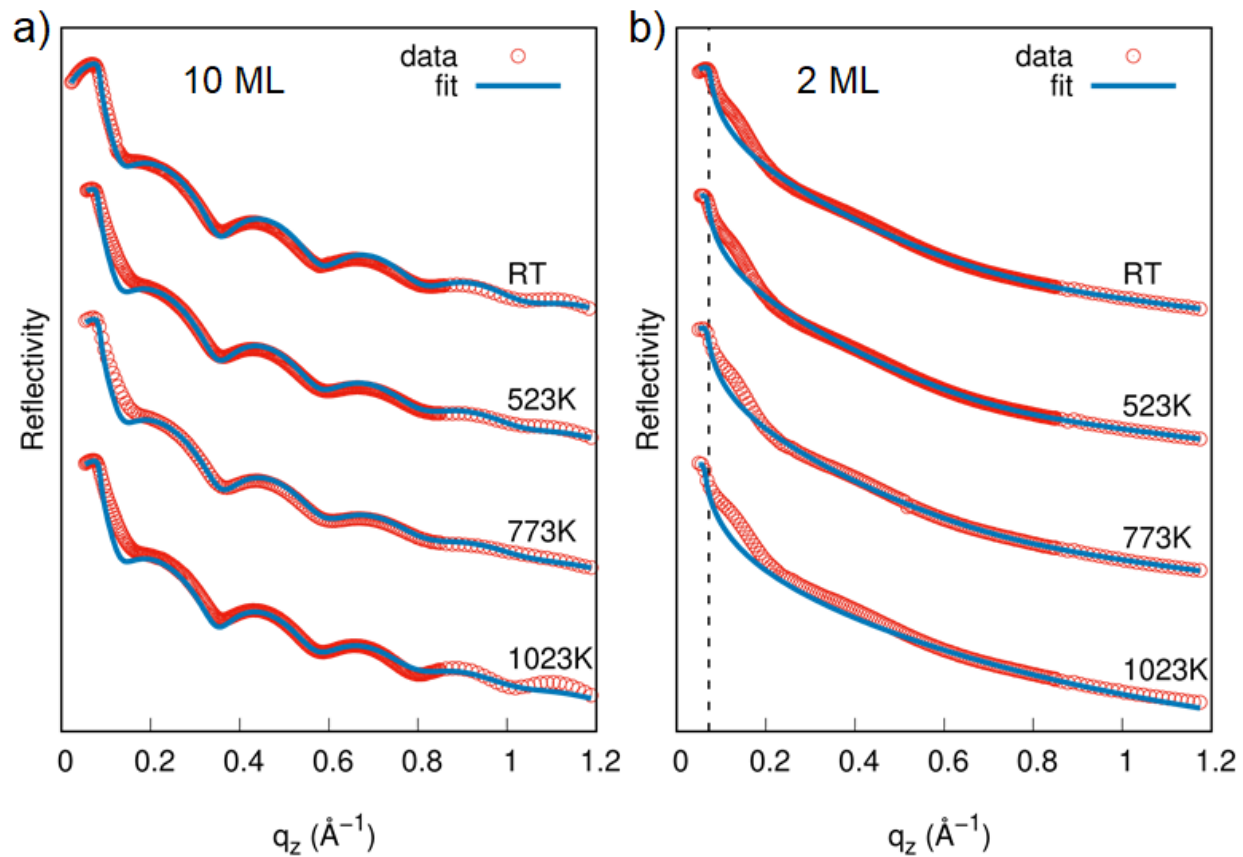


**Figure 3:** XRR profiles (red dots) for a) 10 ML and b) 2 ML cerium oxide films after the thermal treatment at different temperatures and corresponding fits (red curves).

Further information about the out-of-plane structure of the film was obtained from the extended XRR curves, shown in Figure 4. For the 10 ML sample (Figure 4 a) the intense peak at  $l = 3$  r. l. u. can be ascribed to diffraction from the Pt substrate, while the one at  $l = 2.23$  r. l. u. is consistent with diffraction originating from bulk structure of  $\text{CeO}_2$  with a (111) surface orientation. The resulting out-of-plane lattice parameter for the  $\text{CeO}_2$  film is  $c = 3.03 \text{ \AA}$ , a slightly contracted value with respect to the bulk one of  $3.12 \text{ \AA}$ . The position of the  $\text{CeO}_2$  diffraction peak is constant up to 773 K, while after the treatment at 1023 K a very small shift towards smaller  $l$  values is observed (Table 4 and dashed line in Figure 4 a), corresponding to a very small expansion of the out-of-plane lattice parameter ( $c = 3.07 \text{ \AA}$ ). This is qualitatively consistent with the small increase in the concentration of  $\text{Ce}^{3+}$  ions, which have a larger ionic radius compared to  $\text{Ce}^{4+}$  ions. The 2 ML sample (Figure 4 b) instead presents a much more reactive behavior with temperature, compared to the thicker one. Its out-of-plane lattice parameter, estimated from the XRR curves in Figure 4 b, is slightly contracted with respect to the thicker film,  $c = 2.95 \text{ \AA}$ , in agreement with the EXAFS data and with previous results on ultrathin films.<sup>[24]</sup> After the treatment at 773 K the film expands along the  $c$ -axis up to a lattice constant of  $3.00 \text{ \AA}$ , while after the treatment at 1073 K the peak disappears and a further peak at  $l = 1.54$  r.l.u. appears (Table 4). This peak is consistent with the presence of an oriented  $\text{Pt}_5\text{Ce}$  phase with the  $c$ -axis perpendicular to the  $\text{Pt}(111)$  surface, which has already been hypothesized to form, based on the results of the EXAFS and XRR analysis.

The Pt<sub>5</sub>Ce layer presents a slightly expanded out-of-plane lattice parameter ( $c=4.44$  Å) with respect to the bulk material ( $c=4.38$  Å)<sup>[55]</sup>.

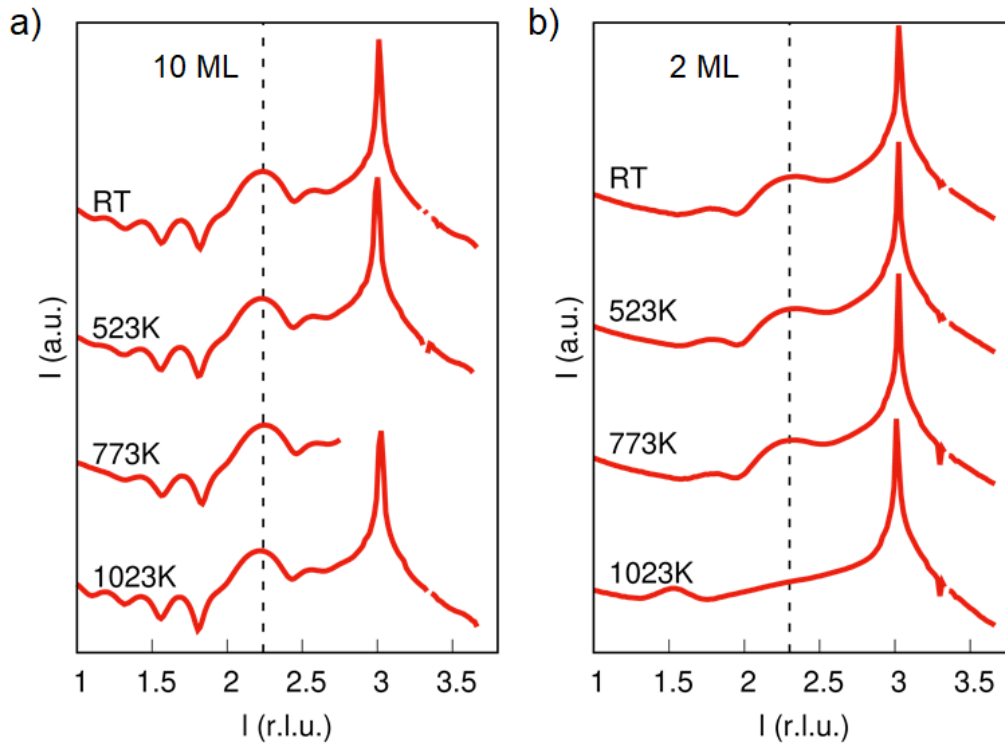


**Figure 4:** Specular XRR profiles a) 10 ML and b) 2 ML cerium oxide films after the thermal treatment at different temperatures.

	Position along $l$ ( r.l.u.)	
	10 ML	2 ML
<b>RT</b>	2.240	2.30
<b>523 K</b>	2.240	2.30
<b>773 K</b>	2.240	2.28
<b>1023 K</b>	2.213	1.53 (Pt <sub>5</sub> Ce)

**Table 4:** Position of the first diffraction peak along the (00l) direction for the 2 and 10 ML samples after the thermal treatment at different temperatures, obtained from the data in Figure 4.

The structural evolution of the film can be also tracked using the in-plane position of the CeO<sub>2</sub> rods or Bragg peaks. Figure 5 reports the projection along the  $h$  axis of the intensities in reciprocal space around the (0.72,

0, 1.44) Bragg peak (shown as sum of intensities in the intervals  $0.68 < h < 0.76$ ,  $-0.02 < k < 0.02$ ,  $1.35 < l < 1.45$ ) for the 10 ML and 2 ML samples after the different treatments. The projection along the  $k$  axis (not shown) does not show any variation of the peak position. The in-plane lattice parameters derived from the position of the (0.72, 0, 1.44) peak are reported in Table 5. The 10 ML film shows a substantially unaltered in-plane lattice parameter, compatible with the bulk one, up to 773 K, while an expansion is observed after the 1023 K treatment. The 2ML film exhibits more significant changes, a small expansion of the lattice parameter is already visible after the treatment at 773 K. At 1023 K the situation drastically changes with the  $\text{CeO}_2$  peak which is significantly shifted to lower  $h$  values, which correspond to a 1.5% expansion of the lattice parameter, and its intensity is significantly decreased, possibly due to the partial formation of a Ce-Pt alloy as observed by XRR and XAFS. The small expansion observed in the plane is compatible with the reduction induced by the treatments.

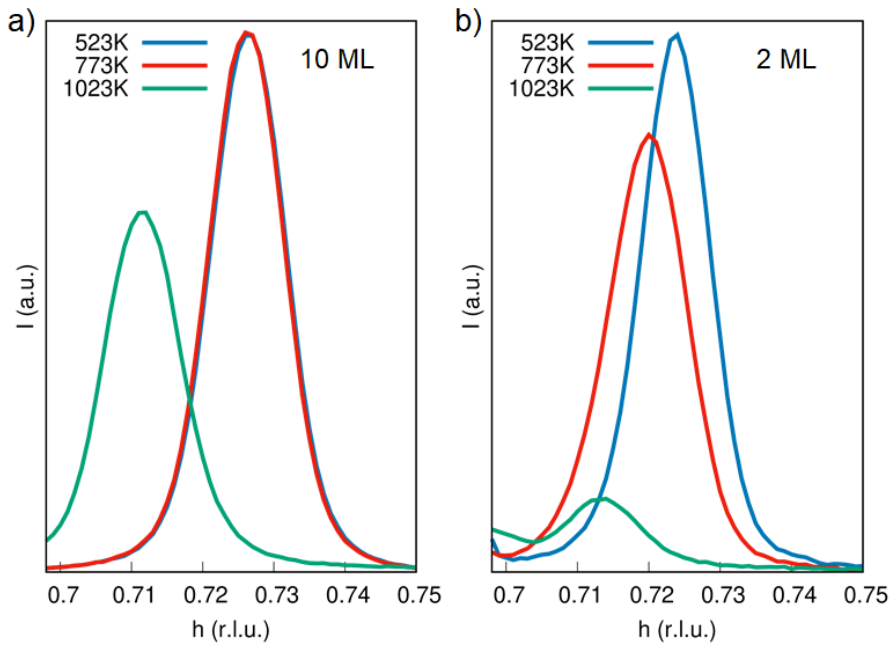


**Figure 5:**  $\text{CeO}_2$  (0.72, 0, 1.44) Bragg peak for the 10 ML (a) and 2 ML (b) samples after the thermal treatments at the different temperatures. The plot is a projection along the  $h$  axis of the diffracted intensities in the reciprocal space volume:  $0.68 < h < 0.76$ ,  $-0.02 < k < 0.02$ ,  $1.35 < l < 1.45$ .



	In-plane lattice parameter (Å)	
	10 ML	2 ML
RT	3.83	3.83
523 K	3.82	3.83
773 K	3.82	3.85
1023 K	3.90	3.89

**Table 5:** In-plane lattice parameter of the surface unit cell for the 10 and 2 ML CeO<sub>2</sub> samples, calculated using the in-plane position of the (0.72, 0 1.44) Bragg peaks.

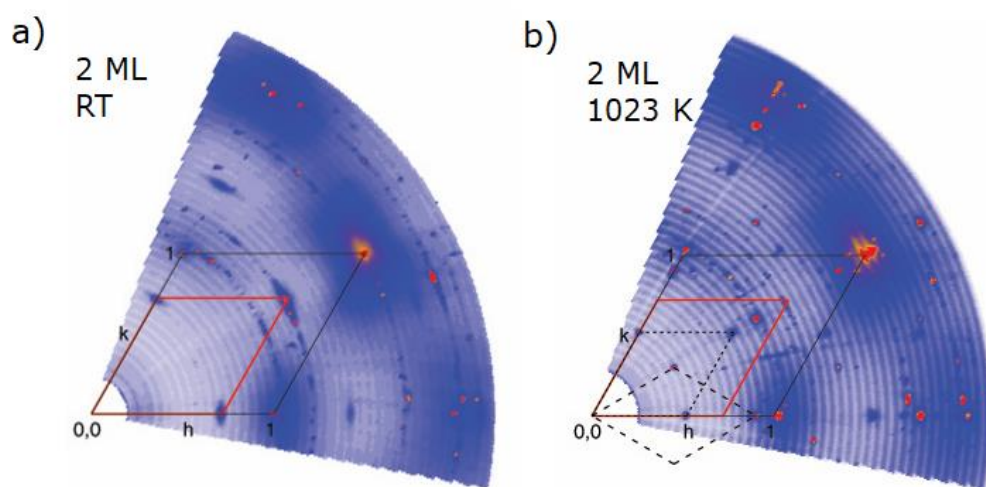


**Figure 6** In-plane SXRD map ( $I=0.3$ ) for the 2 ML sample after oxidation treatment (a) and after the reduction treatment at 1023 K (b). The lines indicate the surface unit cells of Pt (solid black), CeO<sub>2</sub> (solid red) and the two domains of the Pt<sub>5</sub>Ce phase (dashed black). The units reported in the maps refer to the surface unit cell of Pt(111).

To further investigate the new phases formed in the 2 ML sample after high temperature reduction, (h,k) reciprocal space maps before and after the treatment were analyzed (Figure 6). Both maps show intense Pt(111)-related peaks at integer values of h and k (surface unit cell marked with solid black lines), and additional peaks with lower intensity at  $h, k = n \cdot 0.7$ , compatible with the CeO<sub>2</sub>(111) lattice (surface unit cell marked with red lines). After reduction at 1023 K some relevant changes can be observed in the map: while the CeO<sub>2</sub> peaks almost disappear, new sets of peaks can be observed. In particular we identified the presence

of a new structure, compatible with  $\text{CePt}_5$ <sup>[46]</sup> with two orientational domains (surface unit cells marked with dashed black lines in Figure 6 b). One domain is characterized by  $h, k = n \times 0.52$ , with  $n$  being an integer number, and it is compatible with the  $\text{CePt}_5$  phase with a (2x2) periodicity with respect to Pt<sup>[46]</sup>, while the second one is identified by  $h, k = n \times 0.30$  and it can be ascribed to the same structure rotated by  $30^\circ$ , as already observed when the alloy thickness ranges between approximately 4 and 10 atomic layers.<sup>[46, 54, 56, 57]</sup> The in-plane lattice parameter of this phase is slightly contracted with respect to the value reported in literature<sup>[51]</sup> (5.336 Å vs 5.365 Å). Low intensity peaks, surrounding the integer Pt-related spots and arranged with the same symmetry as the substrate, are also evident in Figure 6 b. Such peaks are typical of epitaxial phases with a small lattice mismatch and they originate from the large scale periodicity of the coincidence sites, the so-called moiré pattern, which in this case originates from the superposition of the very close periodicities of the alloy phase and the substrate. The presence of further diffraction peaks after the high temperature treatment derives from an actually more complex situation than the simple picture here described, with the formation of other possible low-dimensional alloy phases, which do not correspond to bulk stable structures.

SXRD allows to complement the information obtained by XAS with an accurate analysis of some of the long range ordered observed phases. First of all, it confirms that the reduction treatment induces significantly less important modifications in thick epitaxial films, as compared to ultrathin films. This represents a further evidence of the role of dimensionality and interaction with the substrate on the reducibility of the material. SXRD is sensitive to periodicities of long-range ordered phases, while XAFS gives complementary information on the average local environment of Ce ions. The observed expansion of the in- and out-of-plane lattice parameters of the long-range ordered  $\text{CeO}_2$  phases with the reduction treatments observed by SXRD is not necessarily in contrast with the contraction of Ce-O average distances, observed by XAFS after reduction, since the latter possibly includes also phases with a low-long range order.

Moreover, SXRD unambiguously demonstrates the formation of a  $\text{CePt}_5$  phase with a high degree of long-range order involving a few atomic layers at the interface with Pt. This highlights the importance of mass exchange processes at the interface between the metal and the oxide in reducing conditions, occurring only when the oxide overlayer has a subnanometric thickness. The observed phase has a non-negligible in-plane compression (0.5%) and an out-of-plane expansion (1.6%), possibly due to low-dimensionality effects, which may be relevant in terms of its possible activity. The formation of a  $\text{Pt}_5\text{Ce}$  alloy can be qualitatively understood by considering the structure of Pt and of the alloy ( $\text{CaCu}_5$ -type structure, see also supporting information, Figure S4). The mechanism which comes into play is likely similar to the one occurring during vacuum annealing of metallic Ce layers deposited on a Pt(111) surface.<sup>[46, 47, 54, 56]</sup> The hexagonal structure of the alloy can in fact be obtained by interdiffusion of Ce ions below the Pt surface, with a mild deformation of the Pt structure, which leads to the formation of alternate  $\text{Pt}_2\text{Ce}$  layers intercalated with layers of Pt atoms, arranged in a close-packed Kagome network, with  $\frac{1}{4}$  atom vacancies which accommodate Ce atoms in the

neighboring layers. The surface termination of the alloy, shown to be a dense Pt layer with an in-plane compressive strain as compared to pure Pt, is responsible for a shift of the binding energy of Pt 4f band with respect to pure Pt, with important consequences on the adsorption and catalytic properties of the compound.<sup>[58, 59]</sup> In particular, Pt<sub>5</sub>Ce alloys were shown to have an outstanding activity towards the oxygen reduction reaction, an extremely important electrochemical reaction occurring at the cathode of fuel cell devices.<sup>[59]</sup> The specific surface structure of the alloy ensures a good stability and a higher chemical activity as compared to pure Pt.<sup>[59, 60]</sup> In analogy, a relative inertness towards CO adsorption has been observed for the alloy phase, as compared to Pt(111), and ascribed to a weakening of the interaction between CO and Pt electronic states.<sup>[57, 61]</sup> The formation of the Pt<sub>5</sub>Ce alloy also in CeO<sub>2</sub>/Pt systems, occurring only at reduced dimensionality, brings important information in view of a better understanding of cerium oxide – Pt catalysts. Atomic exchange processes can in fact occur also under milder reducing conditions, although probably to a more limited spatial extent, with an envisaged relevant role for the functionality of the material, in terms of activity, stability and resistance against surface contamination.

## Conclusions

The present work investigates the local and long range structural modifications induced by thermal treatments in vacuum in cerium oxide supported on Pt(111) single crystals. Cerium oxide films with thickness in the nanometer range do not undergo important structural modifications after reduction by a thermal treatment up to 1023 K in vacuum. On the contrary, the same treatment induces very relevant structural modifications if cerium oxide is in the form of islands of subnanometric thickness supported on the Pt surface. In particular, a contraction of the Ce-O distance by 1% is observed and it is accompanied by the formation of a Ce-Pt alloyed phase with a (2 X 2) periodicity, which is formed via atomic exchange with the support.

## Supporting Information

Supporting Information is available from the Wiley Online Library or from the author.

## Acknowledgements

The work is performed with the financial support of MIUR through PRIN project no. 2015CL3APH.

## References

- [1] A. Trovarelli, P. Fornasiero, *Catalysis by Ceria and Related Materials*, Imperial College Pr., London, **2013**.
- [2] D. J. M. Bevan, *Journal of Inorganic and Nuclear Chemistry* **1955**, *1*, 49.

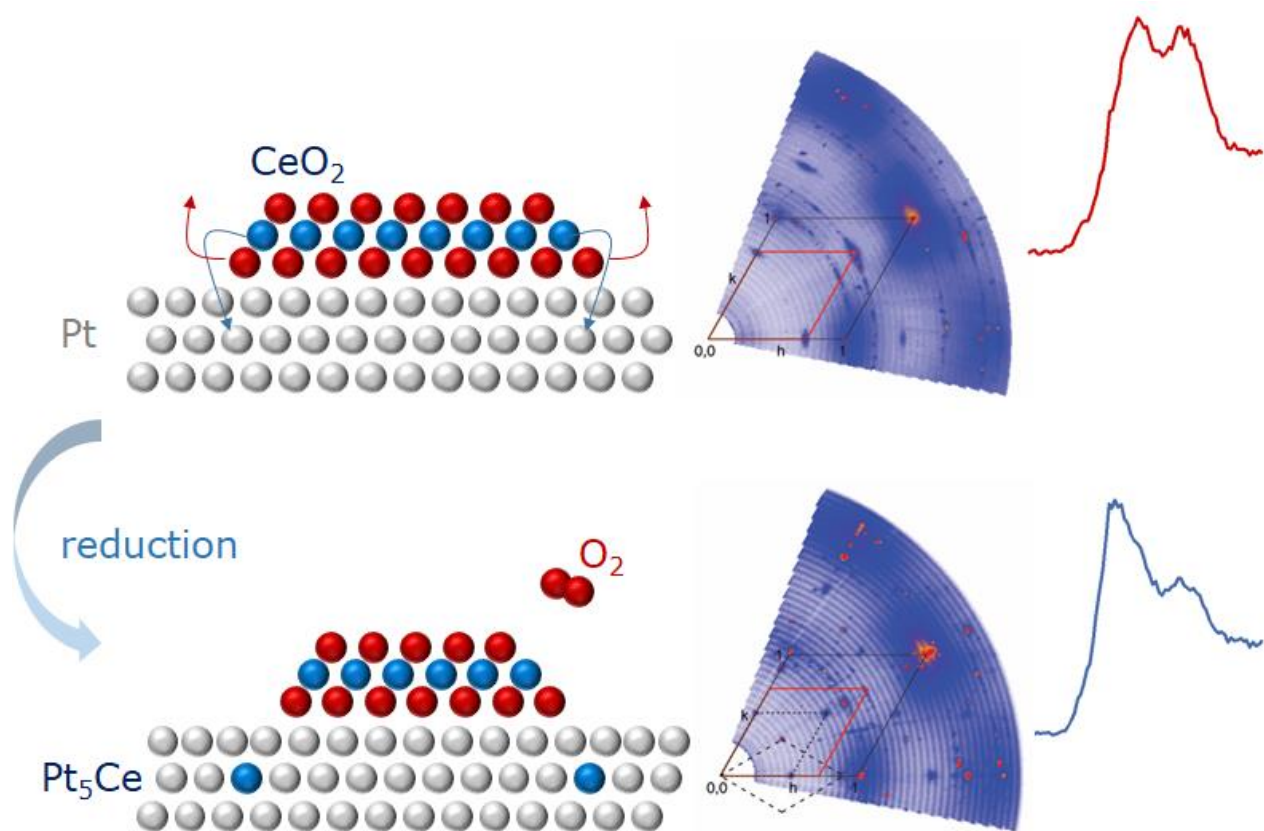
- [3] S. M. Kozlov, I. Demiroglu, K. M. Neyman, S. T. Bromley, *Nanoscale* **2015**, 7, 4361.
- [4] P. Luches, S. Valeri, *Materials* **2015**, 8.
- [5] D. R. Mullins, P. V. Radulovic, S. H. Overbury, *Surf Sci* **1999**, 429, 186.
- [6] B. Kaemena, S. D. Senanayake, A. Meyer, J. T. Sadowski, J. Falta, J. I. Flege, *J Phys Chem C* **2013**, 117, 221.
- [7] F. Esch, S. Fabris, L. Zhou, T. Montini, C. Africh, P. Fornasiero, G. Comelli, R. Rosei, *Science* **2005**, 309, 752.
- [8] J. F. Jerratsch, X. Shao, N. Nilius, H. J. Freund, C. Popa, M. V. Ganduglia-Pirovano, A. M. Burow, J. Sauer, *Phys Rev Lett* **2011**, 106.
- [9] D. C. Grinter, C. Muryn, A. Sala, C.-M. Yim, C. L. Pang, T. O. Menteş, A. Locatelli, G. Thornton, *The Journal of Physical Chemistry C* **2016**, 120, 11037.
- [10] A. Pfau, K. D. Schierbaum, *Surf Sci* **1994**, 321, 71.
- [11] S. Eck, C. Castellarin-Cudia, S. Surnev, M. G. Ramsey, F. P. Netzer, *Surf Sci* **2002**, 520, 173.
- [12] F. Dvorak, O. Stetsovych, M. Steger, E. Cherradi, I. Matolinova, N. Tsud, M. Skoda, T. Skala, J. Myslivecek, V. Matolin, *J Phys Chem C* **2011**, 115, 7496.
- [13] P. Luches, F. Pagliuca, S. Valeri, *Phys Chem Chem Phys* **2014**, 16, 18848.
- [14] H. Wilkens, O. Schuckmann, R. Oelke, S. Gevers, M. Reichling, A. Schaefer, M. Baumer, M. H. Zoellner, G. Niu, T. Schroeder, J. Wollschläger, *Phys Chem Chem Phys* **2013**, 15, 18589.
- [15] J. Höcker, T. O. Menteş, A. Sala, A. Locatelli, T. Schmidt, J. Falta, S. D. Senanayake, J. I. Flege, *Adv Mater Interfaces* **2015**, 2, 1500314.
- [16] C. Castellarin-Cudia, S. Surnev, G. Schneider, R. Podlucky, M. G. Ramsey, F. P. Netzer, *Surf Sci* **2004**, 554, L120.
- [17] T. Duchon, F. Dvorak, M. Aulicka, V. Stetsovych, M. Vorokhta, D. Mazur, K. Veltruska, T. Skala, J. Myslivecek, I. Matolinova, V. Matolin, *J Phys Chem C* **2014**, 118, 357.
- [18] W. Rong, H. Chen, Z. Huang, K. Wu, *The Journal of Physical Chemistry C* **2020**.
- [19] P. Luches, F. Pagliuca, S. Valeri, *J Phys Chem C* **2011**, 115, 10718.
- [20] P. Luches, G. Gasperi, M. Sauerbrey, S. Valeri, J. Falta, J. I. Flege, *Front. Chem.* **2019**, 7, 57.
- [21] H. Wilkens, O. Schuckmann, R. Oelke, S. Gevers, A. Schaefer, M. Bäumer, M. H. Zoellner, T. Schroeder, J. Wollschläger, *Appl Phys Lett* **2013**, 102, 111602.
- [22] G. E. Murgida, V. Ferrari, A. M. Llois, M. V. Ganduglia-Pirovano, *Physical Review Materials* **2018**, 2, 083609.
- [23] J. I. Flege, B. Kaemena, S. Gevers, F. Bertram, T. Wilkens, D. Bruns, J. Batjer, T. Schmidt, J. Wollschläger, J. Falta, *Phys Rev B* **2011**, 84.
- [24] P. Luches, F. Pagliuca, S. Valeri, F. Boscherini, *J Phys Chem C* **2013**, 117, 1030.
- [25] C. Paun, O. V. Safonova, J. Szlachetko, P. M. Abdala, M. Nachtegaal, J. Sa, E. Kleymenov, A. Cervellino, F. Krumeich, J. A. van Bokhoven, *The Journal of Physical Chemistry C* **2012**, 116, 7312.
- [26] A. Longo, L. F. Liotta, G. Pantaleo, F. Giannici, A. M. Venezia, A. Martorana, *The Journal of Physical Chemistry C* **2012**, 116, 2960.
- [27] I. K. Robinson, D. J. Tweet, *Reports on Progress in Physics* **1992**, 55, 599.
- [28] J. Hocker, J.-O. Krispeneit, T. Schmidt, J. Falta, J. I. Flege, *Nanoscale* **2017**, 9, 9352.
- [29] F. d'Acapito, A. Trapananti, A. Puri, *Journal of Physics: Conference Series* **2016**, 712, 012021.
- [30] S. Pascarelli, F. Boscherini, F. D'Acapito, J. Hrdy, C. Meneghini, S. Mobilio, *Journal of Synchrotron Radiation* **1996**, 3, 147.
- [31] F. Pagliuca, P. Luches, S. Valeri, *Surf Sci* **2013**, 607, 164.
- [32] G. Gasperi, L. Amidani, F. Benedetti, F. Boscherini, P. Glatzel, S. Valeri, P. Luches, *Phys Chem Chem Phys* **2016**, 18, 20511.
- [33] J. S. P. Cresi, M. Chiara Spadaro, S. D'Addato, S. Valeri, L. Amidani, F. Boscherini, G. Bertoni, D. Deiana, P. Luches, *Nanotechnology* **2017**, 28, 495702.
- [34] P. Nachimuthu, W.-C. Shih, R.-S. Liu, L.-Y. Jang, J.-M. Chen, *Journal of Solid State Chemistry* **2000**, 149, 408.
- [35] K. O. Kvashnina, S. M. Butorin, P. Glatzel, *Journal of Analytical Atomic Spectrometry* **2011**, 26, 1265.
- [36] B. Ravel, M. Newville, *Journal of Synchrotron Radiation* **2005**, 12, 537.
- [37] A. L. Ankudinov, B. Ravel, J. J. Rehr, S. D. Conradson, *Phys Rev B* **1998**, 58, 7565.
- [38] J. A. Solera, J. García, M. G. Proietti, *Phys Rev B* **1995**, 51, 2678.

- [39] E. Fonda, D. Andreatta, P. E. Colavita, G. Vlaic, *Journal of Synchrotron Radiation* **1999**, 6, 34.
- [40] S. Roobol, W. Onderwaater, J. Drnec, R. Felici, J. Frenken, *Journal of Applied Crystallography* **2015**, 48, 1324.
- [41] P. Luches, L. Giordano, V. Grillo, G. C. Gazzadi, S. Prada, M. Campanini, G. Bertoni, C. Magen, F. Pagliuca, G. Pacchioni, S. Valeri, *Adv Mater Interfaces* **2015**, 2, 1500375.
- [42] T. X. T. Sayle, S. C. Parker, C. R. A. Catlow, *Surf Sci* **1994**, 316, 329.
- [43] P. Luches, G. Gasperi, M. Sauerbrey, S. Valeri, J. Falta, J. I. Flege, *Frontiers in Chemistry* **2019**, 7, 57.
- [44] C. Praetorius, M. Zinner, A. Köhl, H. Kießling, S. Brück, B. Muenzing, M. Kamp, T. Kachel, F. Choueikani, P. Ohresser, F. Wilhelm, A. Rogalev, K. Fauth, *Phys Rev B* **2015**, 92, 045116.
- [45] C. Loschen, S. T. Bromley, K. M. Neyman, F. Illas, *J Phys Chem C* **2007**, 111, 10142.
- [46] C. J. Baddeley, A. W. Stephenson, C. Hardacre, M. Tikhov, R. M. Lambert, *Phys Rev B* **1997**, 56, 12589.
- [47] U. Berner, K. D. Schierbaum, *Phys Rev B* **2002**, 65.
- [48] G. Gasperi, P. Luches, C. Barth, *The Journal of Physical Chemistry C* **2018**, 122, 25954.
- [49] J. A. Blanco, L. Fernández Barquín, D. Gignoux, J. C. Gómez Sal, J. Rodríguez-Carvajal, J. Rodríguez Fernández, *Journal of Magnetism and Magnetic Materials* **1992**, 108, 51.
- [50] J. L. Moriarty, Jr, J. E. Humphreys, R. O. Gordon, N. C. Baenziger, *Acta Crystallographica* **1966**, 21, 840.
- [51] D. T. Adroja, S. K. Malik, B. D. Padalia, R. Vijayaraghavan, *Solid State Communications* **1989**, 71, 649.
- [52] S. Tsunekawa, R. Sivamohan, S. Ito, A. Kasuya, T. Fukuda, *Nanostructured Materials* **1999**, 11, 141.
- [53] M. Bjorck, G. Andersson, *Journal of Applied Crystallography* **2007**, 40, 1174.
- [54] J. Kemmer, C. Praetorius, A. Krönlein, P.-J. Hsu, K. Fauth, M. Bode, *Phys Rev B* **2014**, 90, 195401.
- [55] W. Bronger, *Journal of the Less Common Metals* **1967**, 12, 63.
- [56] J. Tang, J. M. Lawrence, J. C. Hemminger, *Phys Rev B* **1993**, 48, 15342.
- [57] J. M. Essen, C. Becker, K. Wandelt, *e-Journal of Surface Science and Nanotechnology* **2009**, 7, 421.
- [58] C. Praetorius, M. Zinner, G. Held, K. Fauth, *Phys Rev B* **2015**, 92, 195427.
- [59] P. Malacrida, M. Escudero-Escribano, A. Verdaguer-Casadevall, I. E. L. Stephens, I. Chorkendorff, *Journal of Materials Chemistry A* **2014**, 2, 4234.
- [60] V. Tripkovic, J. Zheng, G. A. Rizzi, C. Marega, C. Durante, J. Rossmeisl, G. Granozzi, *ACS Catalysis* **2015**, 5, 6032.
- [61] B. Vermang, M. Juel, S. Raaen, *Phys Rev B* **2006**, 73, 033407.

ToC text:

Cerium oxide nanoislands supported on platinum undergo important structural modifications during reduction treatments. A contraction of the Ce-O distance is observed accompanied by the formation of a long-range ordered Pt<sub>5</sub>Ce alloy phase at the interface. On the contrary, the structural modifications induced by the same treatment in a continuous film with a thickness of several atomic layers are negligible.

ToC figure:



ToC keyword: cerium oxide ultrathin films